Journal of Theoretical Biology 581 (2024) 111737

Contents lists available at ScienceDirect

Journal of Theoretical Biology

journal homepage: www.elsevier.com/locate/yjtbi

A mathematical model of biofilm growth and spread within plant xylem: Case study of *Xylella fastidiosa* in olive trees

N.C. Walker [a], S.M. White [b], S.A. Ruiz [a], D. McKay Fletcher [a,c], M. Saponari [d], T. Roose [a,*]

[a] Bioengineering Sciences Research Group, Department of Mechanical Engineering, School of Engineering, Faculty of Engineering and Physical Sciences, University of Southampton, SO17 1BJ, UK
[b] UK Centre for Ecology & Hydrology, Maclean Building, Benson Lane, Crowmarsh Gifford, Wallingford, Oxfordshire OX10 8BB, UK
[c] Rural Economy Environment and Society Research Group, SRUC, Edinburgh EH9 3JG, UK
[d] Istituto per la Protezione Sostenibile delle Piante, CNR, Bari, Italy

ARTICLE INFO

Keywords:
Xylem-limited bacterial pathogen
Multiphase model
Biofilm formation
Xylella fastidiosa
Olive

ABSTRACT

Xylem-limited bacterial pathogens cause some of the most destructive plant diseases. Though imposed measures to control these pathogens are generally ineffective, even among susceptible taxa, some hosts can limit bacterial loads and symptom expression. Mechanisms by which this *resistance* is achieved are poorly understood. In particular, it is still unknown how differences in vascular structure may influence biofilm growth and spread within a host. To address this, we developed a novel theoretical framework to describe biofilm behaviour within xylem vessels, adopting a polymer-based modelling approach. We then parameterised the model to investigate the relevance of xylem vessel diameters on *Xylella fastidiosa* resistance among olive cultivars. The functionality of all vessels was severely reduced under infection, with hydraulic flow reductions of 2–3 orders of magnitude. However, results suggest wider vessels act as biofilm incubators; allowing biofilms to develop over a long time while still transporting them through the vasculature. By contrast, thinner vessels become blocked much earlier, limiting biofilm spread. Using experimental data on vessel diameter distributions, we were able to determine that a mechanism of resistance in the olive cultivar Leccino is a relatively low abundance of the widest vessels, limiting *X. fastidiosa* spread.

1. Introduction

Plant pathogenic bacteria are responsible for many serious plant diseases around the world (see Fig. 2 of Vidhyasekaran (2002)). Some of the most important are those that colonise host vasculature (Mansfield et al., 2012), e.g. *Xylella fastidiosa*, responsible for a recent olive disease outbreak in Puglia; an important olive-growing area in Southern Italy (Saponari et al., 2013; Saponari et al., 2019). Vasculature functionality is essential for plant survival, transporting both the reactants necessary for photosynthesis, and resulting photosynthetic products, through the plant. Additionally, the nutrient profile of the vascular environment ensures sustained pathogen proliferation, and its extensive network structure facilitates a rapid systemic distribution of the pathogen in infected plants (Bové and Garnier, 2002).

Plants have two primary vascular tissues: xylem and phloem. Though the phloem is much richer in nutrients, most plant vascular pathogens inhabit the xylem, likely due to its relative ease of access (Yadeta et al., 2013). Symptoms of diseases caused by xylem-limited bacterial pathogens are non-specific, with their duration and severity depending not only on host-pathogen species and association (Yadeta et al., 2013), but also factors relating to the environmental conditions (Rapicavoli et al., 2018). In the most severe cases, plants become stunted, wilt, and eventually die (Yadeta et al., 2013). In general, signs of disease induced by xylem-limited bacterial pathogens appear to be caused by bacterial biofilms and structures formed in the plant defence, both acting to restrict xylem flow. After initial dispersal, local colonies aggregate on xylem vessel walls, directly blocking sap ascent. These biofilm structures are robust, protecting the bacterial communities from stresses imposed by the fluid environment (Hall-Stoodley et al., 2004). However, particularly in late stages of development, they provide significant impedance to xylem flow with negative impact on the host.

Some host genotypes are *resistant* (Agrios, 2005), being able to

* Corresponding author: Bioengineering Sciences Research Group, Department of Mechanical Engineering, School of Engineering, Faculty of Engineering and Physical Sciences, University of Southampton, University Road, Southampton SO17 1BJ, UK.
E-mail address: T.Roose@soton.ac.uk (T. Roose).

https://doi.org/10.1016/j.jtbi.2024.111737
Received 1 February 2023; Received in revised form 16 November 2023; Accepted 10 January 2024
Available online 25 January 2024

maintain lower bacterial loads and limit symptom expression under infection. For many plant vascular diseases, resistant plants present the most promising means for control (Yadeta et al., 2013). Correlations between particular plant traits and disease resistance have been identified for a number of pathosystems with variable host susceptibility. Some traits relate to vascular anatomy; for example, differences in xylem vessel diameters have been correlated with resistance to *X. fastidiosa* in a number of host taxa (Chatelet et al., 2011; Sabella et al., 2019; Walker et al., 2022). However, the mechanisms by which these differences influence biofilm structure and spread, and resulting impacts on vessel functionality, are poorly understood. Though general hypotheses as to how vessel sizes could act as a resistance mechanism have been made (Chatelet et al., 2011; Sabella et al., 2019), no evidence has been given, and thus they remain only speculative.

Mathematical models provide an avenue for investigating dynamics of biological phenomena beyond experimental capability. A small number of theoretical descriptions of biofilms in xylem exist in the literature (Cogan et al., 2013; Whidden et al., 2015), noting that both pertain specifically to describing xylem infection by *X. fastidiosa* bacteria. These models focus on capturing the interaction between motile and biofilm-associated bacteria under dynamic xylem flow. Investigated solutions focus on the relative importance of detachment and attachment processes in *X. fastidiosa* biofilm structure. However, due to the model complexity, examined solutions correspond only to situations with zero xylem fluid velocity. As a result, biofilm-flow interactions that would occur under realistic flow regimes are not captured. Thus, these models are limited when inferring the impact of biofilm on xylem functionality and assessing the potential for pathogen spread in the vasculature.

Though biofilm model development has been limited in the context of bacterial plant pathogens, general biofilm model development has received significant attention. In particular, a number of models have focused on capturing biofilm growth and development within a fluid environment (Klapper and Dockery, 2002; Cogan and Keener, 2004; Cogan and Keener, 2005; Zhang et al., 2008; Zhang et al., 2008; Cogan and Guy, 2010; Winstanley et al., 2011). Some treat the biofilm as solid biomass (Eberl et al., 2000; Eberl et al., 2001), with biomass spreading defined according to the presence of a limiting nutrient substrate. Though these models provide useful predictions of where biofilm heterogeneities may occur due to the evolving nutrient environment, they assume an initial biofilm profile, and do not capture the mechanical influence of the hydraulic environment on biofilm structure. Other models treat biofilm as a visco-elastic body (Klapper and Dockery, 2002), also assuming an initial biofilm profile, but retaining a mechanical influence of the fluid environment on the biofilm. More recent models consider the biofilm as a polymer gel, for which the biofilm architecture and subsequent dynamics evolve according to a consideration of the free-energy associated with the arrangement of extracellular polymeric substance (EPS) molecules (Cogan and Keener, 2004; Cogan and Keener, 2005; Zhang et al., 2008; Zhang et al., 2008; Cogan and Guy, 2010; Winstanley et al., 2011).

The goal of this paper is to develop a novel theoretical modelling framework that can capture the interaction between biofilm and dynamic xylem fluid flow explicitly. We present a multidimensional multiphase continuum model, representing biofilm in a xylem vessel using a water-polymer gel free-energy description. We adopt this approach due to its limited reliance on experimental parameters, and because it doesn't require an initial biofilm profile as an input. Model solutions are compared to microfluidic experiments of biofilm aggregation, showing good qualitative agreement with observed dynamics. We then use the model to investigate the following hypotheses relating to olive cultivar resistance to the pathogen *X. fastidiosa*:

1. The presence of *X. fastidiosa* biofilms in the xylem impairs sap flow.
2. Wider vessels act as incubators for biofilms to proliferate, whilst maintaining biofilm spread through the vasculature.
3. Narrower vessels are rapidly blocked by biofilms, limiting their contribution to within-host pathogen spread.

These hypotheses were tested based on measurements from theoretical experiments carried out via model simulation. In these simulations, a range of set-ups were used, corresponding to different vessel diameters, to assess the impact of vessel diameter on within-host infection dynamics.

2. Methods

2.1. General model description

Our model is designed to capture the dynamics within a xylem vessel of a transpiring tree infected by pathogenic bacterial biofilms (Fig. 1).

Fluid dynamics in the xylem can be understood *via* the *cohesion-tension theory* (Dixon and Joly, 1895). During the day, stomata open so that carbon dioxide can enter leaves at sufficient rates to support sunlight driven photosynthesis. When stomata are open, water is lost via transpiration. This results in a pull on the water columns in the xylem, maintaining a continuous flow through the vasculature (Fig. 1B). At night, stomata close to avoid excessive water loss when the plant cannot photosynthesise. During this time, water in the xylem is held under tension (Fig. 1A). An individual vessel in an infected tree will experience this natural cycle (Fig. 1C), as long as a blockage-free path exists to the stomata. In our model, we apply a pressure condition to reflect this diurnal pattern and consider infection dynamics only up until the biofilm spans the width at the top of the vessel.

We describe the contents of a subsection of an infected xylem vessel as a mathematical domain $\widetilde{\Omega}$ described by a single set of variables (Fig. 1D). To capture infection dynamics, we start from a situation where the xylem has been inoculated with a small amount of bacteria. We assume the modelled vessel section to be occupied by a polymer-water mixture describing the biofilm, referred to as *polymer-gel,* and xylem sap, which, approximated by water fluid properties, is now referred to as *free-water*. This approximation is assumed on the basis that xylem sap contains very limited amounts of organic compounds (Krishnan et al., 2011). The influence of bacteria is present in the growth term describing the production of the polymer-gel. Otherwise, we assume hydrated EPS to be dominant in determining instantaneous biofilm structure. This assumption is made on the basis that EPS can be considered the primary biofilm matrix material (Donlan, 2002), accounting for 50–90% of the biofilm's total organic carbon (Evans, 2000). We acknowledge that, though not included in our model, most bacteria have external appendages allowing them to perform some level of controlled motility. Some bacteria have flagella; long filamentous appendages facilitating a controlled 'swimming' motion (Kearns, 2010). Others, including *X. fastidiosa*, have shorter rigid appendages, IV-pili, allowing them to control their direction of motion *via* a *twitching* movement (Mattick, 2002). However, at the spatial scales considered, we consider the influence of individual driven motion to be negligible.

2.2. Model formulation

2.2.1. Continuity of fluids

We prescribe the following continuity equations for the volume fractions of polymer-gel and free-water respectively:

$$\partial_t \phi + \widetilde{\nabla}\cdot\left(\phi \widetilde{\boldsymbol{u}}_b\right) = \widetilde{G}_1(\phi), \tag{1}$$

$$\partial_t (1-\phi) + \widetilde{\nabla}\cdot\left((1-\phi)\widetilde{\boldsymbol{u}}_w\right) = -\widetilde{G}_2(\phi). \tag{2}$$

ϕ denotes the local polymer-gel volume fraction; $\phi = 0$ indicates free-water, and $\phi = 1$ indicates regions of pure polymer-gel. The velocity

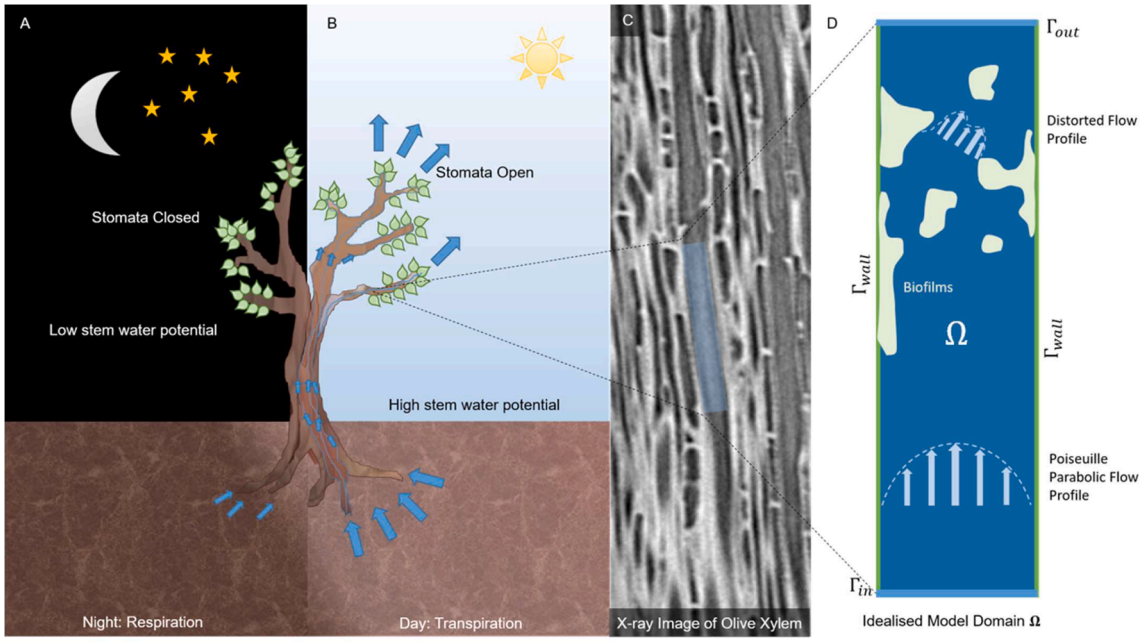

Fig. 1. Model Set-up. A and B illustrate a diurnal cycle in an olive tree. At night (A), stomata close, reducing the pressure gradient across the xylem to almost zero. This results in almost no flow through the stem. In the day (B), stomata open, increasing the pressure gradient. This results in a steady flow through the whole active xylem network. A varying pressure gradient is applied across the model domain to emulate this natural cycle. C highlights a section of xylem vessel within the vasculature of an olive stem, imaged using X-Ray Computed Tomography (Walker et al., 2022). This vessel structure is represented in the model, as illustrated in D where the modelled xylem flow and its interaction with the biofilm is described pictorially. Light green illustrates polymer-gel, and blue, free-water.

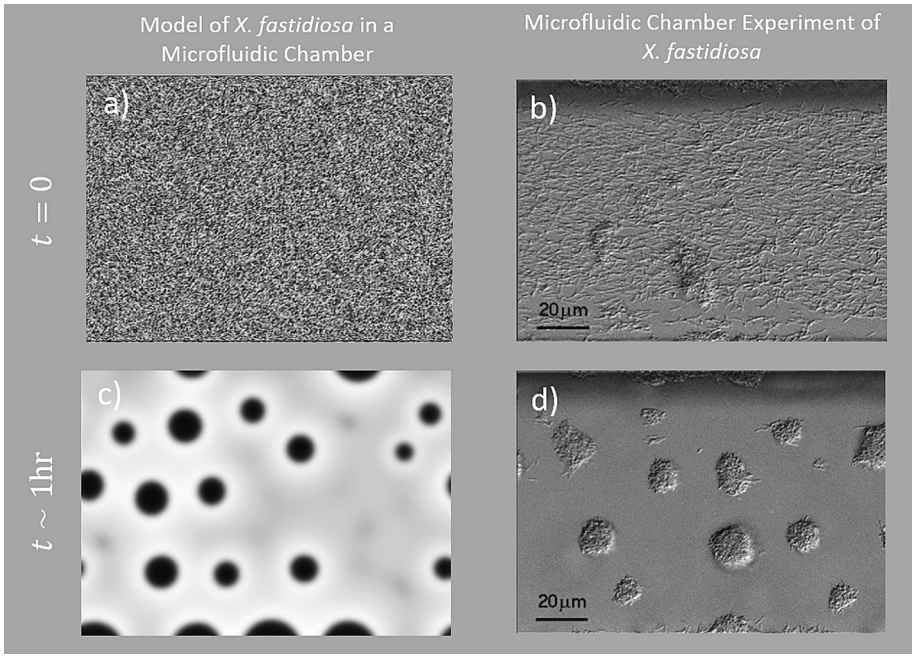

Fig. 2. Comparison of Model (a, c) and Real (b, d De La Fuente et al., 2008) *X. fastidiosa* Biofilm Aggregation.

fields of polymer-gel and free-water are denoted $\widetilde{\boldsymbol{u}}_b$ [m s^{-1}] and $\widetilde{\boldsymbol{u}}_w$ [m s^{-1}] respectively. $\widetilde{G}_1(\phi)$ accounts for biofilm growth, and $\widetilde{G}_2(\phi)$ accounts for both water consumption by the bacteria and biofilm swelling. The dependence of $\widetilde{G}_1$ on ϕ accounts for the assumption that bacteria and EPS can only be generated from bacteria already present in the domain, *i.e.* no more bacteria are inoculated during the simulated time interval. The dependence of $\widetilde{G}_2$ on ϕ accounts for the fact that the two represented phenomena only occur where bacterial biofilm is already present. Eqs. (1) and (2) formulate the rate of change of local volume fractions in terms of convection and biofilm growth.

Adding (1) and (2) gives us the following condition for the whole system:

$$\widetilde{\nabla}\cdot\widetilde{\boldsymbol{u}} = \widetilde{G}_1(\phi) - \widetilde{G}_2(\phi), \tag{3}$$

where $\widetilde{\boldsymbol{u}} = \phi\widetilde{\boldsymbol{u}}_b + (1-\phi)\widetilde{\boldsymbol{u}}_w$ is the average velocity of the entire polymer-gel-free-water fluid mixture. Eq. (3) will be retained in the model to

ensure mass conservation within the domain. Eqs. (1) and (2) will be reformulated later in terms of the domain average velocity $\widetilde{\boldsymbol{u}}$.

2.2.2. Free-energy formulation

We derive organisation dynamics using a free-energy description of biofilm using its characterisation as a polymer-gel. The free-energy density of the polymer-gel, $\widetilde{f}$, describes its thermodynamic state, and determines its mixing behaviour with the free-water. Ultimately, our free-energy description should ensure biofilm aggregation is maintained in the model, *i.e.* if the domain is brought into a mixed state, it should rapidly separate into polymer-gel and free-water. Conditions under which this criterion is met are discussed in the Supplementary Information (S1). Before deriving a free-energy expression we note that, to ensure numerical stability, simulations are run using a polynomial approximation to $\widetilde{f}$. Again, this is discussed in the Supplementary Information (S4).

The free-energy density of the polymer-gel $\widetilde{f}$ [J m^{-3}] consists of three components (following Flory, 1953): an entropic mixing term ($\widetilde{f}_m$ [J m^{-3}]), an energetic interaction term ($\widetilde{f}_i$ [J m^{-3}]), and an elastic term ($\widetilde{f}_{el}$ [J m^{-3}]). The full derivation of these terms according to the theory of Flory (1953) is given in the Supplementary Information (S2). The entropic mixing term accounts for the tendency of a system to become more disorganised because of the second law of thermodynamics. This expression relates to the number of potential configurations of molecules in the system, and is given by $\widetilde{f}_m = \frac{Tk_B}{V_p}((1-\phi)\ln(1-\phi))$, where T [K] is temperature, k_B [J K^{-1}] is the Boltzmann constant, and V_p [m^3] is the molecular volume of a polymer segment. The interaction energy of mixing, an enthalpy term, accounts for the internal work associated with the mixture. It is expressed as $\widetilde{f}_i = \frac{Tk_B}{V_p}(\chi\phi(1-\phi))$, where χ [−] denotes the Flory polymer chain-water interaction parameter. This expression corresponds to the energetic interaction between neighbouring molecules. Lastly, an elastic energy term is considered. Polymer chains are in a different energetic state when they are stretched compared to when they are coiled. This term corresponds to the natural stretching of overlapping polymer chains in the biofilm network. It is given as $\widetilde{f}_{el} = -\frac{Tk_B}{V_pN_x}\left(\phi - \phi_0 + \frac{1}{2}\phi\ln\left(\frac{\phi_0}{\phi}\right)\right)$, where N_x [−] is the number of water molecules between polymer chain crosslinks, and ϕ_0 [−] is the initial polymer-gel volume fraction, causing an initial amount of stretching. The total free-energy density of the polymer-gel is given as the sum of these three terms; $\widetilde{f} = \widetilde{f}_m + \widetilde{f}_i + \widetilde{f}_{el}$.

Along with free-energy terms associated internally to the polymer-gel, an interfacial free-energy term is also considered. This term corresponds to the influence of interface energy acting between free-water and polymer-gel. Since we represent the two phases as dissimilar fluids, this term is given analogously to the Young-Laplace equation;

$$\widetilde{f}_s = \frac{\widetilde{\kappa}}{2}\|\widetilde{\nabla}\phi\|^2, \tag{4}$$

where $\widetilde{\kappa}$ [N] defines the transition zone between free-water and polymer-gel. Thus, the total bulk free-energy of the system is given by

$$\widetilde{E}(\phi) = \int_{\widetilde{\Omega}}\left(\widetilde{f}(\phi) + \frac{\widetilde{\kappa}}{2}\|\widetilde{\nabla}\phi\|^2\right)\mathrm{d}\widetilde{\boldsymbol{x}}. \tag{5}$$

The terms of $\widetilde{E}$ [J] correspond to free-energies associated with the biofilm and its interface. However, there are other energetic terms needed to resolve the domain dynamics. Those terms are concerned with the momentum of the respective phases. Firstly, energy is lost due to drag between polymer-gel and free-water. This is represented by

$$\Delta\widetilde{E}_{\mathrm{drag}} = \frac{1}{2}\widetilde{\zeta}\left|\widetilde{\boldsymbol{u}}_b - \widetilde{\boldsymbol{u}}_w\right|^2, \tag{6}$$

where $\widetilde{\zeta}$[N s m^{-4}] represents a drag coefficient. In addition, energy is lost through shear and tensile stresses between adjacent fluid layers. This is represented by

$$\Delta\widetilde{E}_{\mathrm{stress}} = -(\widetilde{\nabla}\cdot\widetilde{\sigma})\cdot\widetilde{\boldsymbol{u}}, \tag{7}$$

where the stress tensor $\widetilde{\sigma}$ is given by

$$\widetilde{\sigma} = \widetilde{\eta}\left(\widetilde{\nabla}\widetilde{\boldsymbol{u}} + (\widetilde{\nabla}\widetilde{\boldsymbol{u}})^T\right) - \widetilde{\Lambda}\boldsymbol{I}. \tag{8}$$

The first term in the stress tensor represents a viscous stress, where bulk viscosity $\widetilde{\eta}$ [Pa s] is defined as $\widetilde{\eta} = \widetilde{\eta}_b\phi + \widetilde{\eta}_w(1-\phi)$; a linear interpolation between gel viscosity $\widetilde{\eta}_b$ [Pa s] and water viscosity $\widetilde{\eta}_w$ [Pa s]. A Lagrange multiplier, $\widetilde{\Lambda}$ [−], is included in the stress tensor due to the fact that the free-energy terms derived within this theoretical framework (see Flory (1953)) have a number of underlying assumptions that can mean some imposed fluid properties, such as incompressibility of phases, do not hold. $\widetilde{\Lambda}$ acts as a generalised fluid pressure that ensures they are upheld.

The equations of motion are derived using Onsager's principle (Onsager, 1931a,b), an analogue of the principle of least action. In isothermal conditions, this variational principle reduces to a form termed *the principle of least energy dissipation*, stating that any dynamics is expected to follow a path resulting in the minimum total dissipation of energy from the system. An in depth discussion of the method is found in Hillert and Ågren (2006). In order to invoke this principle, we consider the total energy dissipation for the system, given by the following Rayleighian

$$\widetilde{R} = \partial_{\widetilde{t}}\widetilde{E} + \int_{\widetilde{\Omega}}\left\{\frac{1}{2}\widetilde{\zeta}\left|\widetilde{\boldsymbol{u}}_b - \widetilde{\boldsymbol{u}}_w\right|^2 - (\widetilde{\nabla}\cdot\widetilde{\sigma})\cdot\widetilde{\boldsymbol{u}}\right\}\mathrm{d}\widetilde{\boldsymbol{x}}, \tag{9}$$

where the change in the free-energy, after applying Green's identity and some algebra, is defined in terms of a chemical potential $\widetilde{\mu}$ (Doi, 2013);

$$\frac{\partial\widetilde{E}}{\partial\widetilde{t}} = \int_{\widetilde{\Omega}}\left(\widetilde{\mu}\cdot\widetilde{\boldsymbol{u}}_b\right)d\widetilde{\boldsymbol{x}}, \tag{10}$$

where

$$\widetilde{\mu} = \partial_{\phi}\widetilde{f} - \widetilde{\kappa}\widetilde{\nabla}^2\phi. \tag{11}$$

Adopting this notation and setting the functional derivatives $\frac{\delta\widetilde{R}}{\delta\widetilde{\boldsymbol{u}}_i}$ to zero results in the following two-phase Darcy-like flow equations:

$$\phi\{\widetilde{\nabla}\widetilde{\mu} - \widetilde{\nabla}\cdot\widetilde{\sigma}\} + \widetilde{\zeta}\left(\widetilde{\boldsymbol{u}}_b - \widetilde{\boldsymbol{u}}_w\right) = 0, \tag{12}$$

and

$$(1-\phi)\{-\widetilde{\nabla}\cdot\widetilde{\sigma}\} + \widetilde{\zeta}\left(\widetilde{\boldsymbol{u}}_w - \widetilde{\boldsymbol{u}}_b\right) = 0. \tag{13}$$

Adding (12) and (13), we get

$$\widetilde{\nabla}\cdot\widetilde{\sigma} = \phi\widetilde{\nabla}\widetilde{\mu}. \tag{14}$$

Recalling (8), this can be written as

$$\widetilde{\nabla}\cdot\left(\widetilde{\eta}\left(\widetilde{\nabla}\widetilde{\boldsymbol{u}} + (\widetilde{\nabla}\widetilde{\boldsymbol{u}})^T\right)\right) - \widetilde{\nabla}\widetilde{\Lambda} = \phi\widetilde{\nabla}\widetilde{\mu}. \tag{15}$$

Eqs. (15) and (3) correspond to a modified Stokes flow and will describe the bulk motion of the fluid mixture.

Combining (13) and (14), we obtain a Darcy-like description for the movement of the polymer-gel with respect to free-water:

$$\widetilde{\zeta}\left(\widetilde{\boldsymbol{u}}_w - \widetilde{\boldsymbol{u}}_b\right) - (1-\phi)\phi\widetilde{\nabla}\widetilde{\mu} = 0. \tag{16}$$

Using (16), we express the respective gel and water velocities in

terms of the average velocity $\widetilde{\boldsymbol{u}}$:

$$\widetilde{\boldsymbol{u}}_b = \widetilde{\boldsymbol{u}} - \frac{\phi(1-\phi)^2}{\widetilde{\zeta}}\widetilde{\nabla}\widetilde{\mu}, \tag{17}$$

and

$$\widetilde{\boldsymbol{u}}_w = \widetilde{\boldsymbol{u}} + \frac{(1-\phi)\phi^2}{\widetilde{\zeta}}\widetilde{\nabla}\widetilde{\mu}. \tag{18}$$

Finally, substituting these velocity expressions ((17) and (18)) into the volume conservation Equations (1) and (2), we have

$$\partial_t\phi + \widetilde{\nabla}\cdot\left(\phi\left[\widetilde{\boldsymbol{u}} - \frac{\phi(1-\phi)^2}{\widetilde{\zeta}}\widetilde{\nabla}\widetilde{\mu}\right]\right) = \widetilde{G}_1(\phi), \tag{19}$$

$$\partial_t(1-\phi) + \widetilde{\nabla}\cdot\left((1-\phi)\left[\widetilde{\boldsymbol{u}} + \frac{(1-\phi)\phi^2}{\widetilde{\zeta}}\widetilde{\nabla}\widetilde{\mu}\right]\right) = -\widetilde{G}_2(\phi). \tag{20}$$

There is a redundancy among (3), (11), (15), (19) and (20). Thus, to focus on developments of the polymer-gel, we will solve for (19), and not (20). It is clear that (20) can be considered as the difference between (3) and (19), and thus holds automatically if (3) and (19) hold. Eqs. (19) and (11) correspond to a description of two-phase fluid separation and will ensure that gel and water remain separated.

In summary, we will explicitly solve the system of equations defined by (3), (11), (15) and (19). Restating those equations, we solve:

$$\partial_t\phi + \widetilde{\nabla}\cdot\left(\phi\left[\widetilde{\boldsymbol{u}} - \frac{\phi(1-\phi)^2}{\widetilde{\zeta}}\widetilde{\nabla}\widetilde{\mu}\right]\right) = \widetilde{G}_1(\phi), \tag{21}$$

$$\widetilde{\mu} = \partial_{\phi}\widetilde{f} - \widetilde{\kappa}\widetilde{\nabla}^2\phi, \tag{22}$$

$$\widetilde{\nabla}\cdot\left(\widetilde{\eta}\left(\widetilde{\nabla}\widetilde{\boldsymbol{u}} + (\widetilde{\nabla}\widetilde{\boldsymbol{u}})^T\right)\right) - \widetilde{\nabla}\widetilde{\Lambda} = \phi\widetilde{\nabla}\widetilde{\mu}, \tag{23}$$

$$\widetilde{\nabla}\cdot\widetilde{\boldsymbol{u}} = \widetilde{G}_1(\phi) - \widetilde{G}_2(\phi). \tag{24}$$

Ultimately, we want to solve these equations for ϕ, $\widetilde{\boldsymbol{u}}$, $\widetilde{\mu}$ and $\widetilde{\Lambda}$ subject to suitable boundary conditions.

2.3. Boundary conditions

We set up boundary conditions representative of what is understood to happen in xylem vessels. First, we consider conditions imposed on the vessel wall boundary, denoted $\widetilde{\Gamma}_{\text{wall}}$ (see Fig. 1D). As is common to all fluid flows along a solid boundary, we impose no fluid movement at the wall,

$$\widetilde{\boldsymbol{u}}|_{\widetilde{\Gamma}_{wall}} = 0. \tag{25}$$

We also ensure polymer-gel is not lost through the walls by prescribing a zero-flux boundary

$$\boldsymbol{n}\cdot\left(\widetilde{\boldsymbol{u}} - \frac{\phi(1-\phi)^2}{\widetilde{\zeta}}\widetilde{\nabla}\widetilde{\mu}\right)|_{\widetilde{\Gamma}_{wall}} = 0, \tag{26}$$

which, given the no slip condition (21), implies:

$$\boldsymbol{n}\cdot\widetilde{\nabla}\widetilde{\mu}|_{\widetilde{\Gamma}_{wall}} = 0. \tag{27}$$

Finally, we prescribe a contact angle for the polymer-gel fraction, representing the fact that polymer molecules interact with the wall differently from water molecules. This is captured by

$$\boldsymbol{n}\cdot\widetilde{\kappa}\widetilde{\nabla}\phi|_{\widetilde{\Gamma}_{wall}} = \widetilde{\kappa}\|\widetilde{\nabla}\phi\|\cos\theta, \tag{27}$$

where θ [rad] is the prescribed contact angle.

We now present conditions at the inlet and outlet, denoted $\widetilde{\Gamma}_{\text{in}}$ and $\widetilde{\Gamma}_{\text{out}}$ respectively (Fig. 1D). These conditions are based on a few assumptions. The first is that the infection level is similar throughout the vessel length. By this assumption, we assume periodicity of ϕ at inlet and outlet. This also accounts for the choice in the length of modelled vessel section, representing a control vessel sub-length, or length of microfluidic chamber as used in representative *in vitro* experiments (Sternberg et al., 1999; De La Fuente et al., 2008). For our chosen vessel sub-length, we estimate input and output pressures based on empirical measured pressure gradients over plant height. If we changed the sub-length, the inlet and outlet pressures would change to maintain the gradient. For a given pressure gradient across a vessel, a corresponding volume of fluid will move through that vessel over a given time interval independent of the chosen vessel sub-length.

The periodic condition on ϕ and $\widetilde{\nabla}\phi$ is given by

$$\phi|_{\widetilde{\Gamma}_{in}} = \phi|_{\widetilde{\Gamma}_{out}}, \tag{29}$$

and

$$\widetilde{\nabla}\phi|_{\widetilde{\Gamma}_{in}} = \widetilde{\nabla}\phi|_{\widetilde{\Gamma}_{out}}. \tag{30}$$

Pressure conditions are controlled through $\widetilde{\Lambda}$, the Lagrange multiplier representing a combined fluid pressure;

$$\widetilde{\Lambda}|_{\widetilde{\Gamma}_{in}} = \widetilde{p}_{in}(t), \tag{31}$$

and

$$\widetilde{\Lambda}|_{\widetilde{\Gamma}_{out}} = \widetilde{p}_{out}. \tag{32}$$

We take $\widetilde{p}_{in}(t)$ to be a sinusoidal function with a phase of $-\frac{\pi}{2}$ and a period of 24 h (τ_{day}):

$$\widetilde{p}_{in}(t) = \frac{\widetilde{p}_{in,max} - \widetilde{p}_{in,min}}{2} sin\left(\frac{2\pi\tau t}{\tau_{day}} - \frac{\pi}{2}\right) + \frac{\widetilde{p}_{in,max} + \widetilde{p}_{in,min}}{2}. \tag{33}$$

This corresponds to a diurnal change in the pressure gradient across the vessel (Fig. 1 A,B). The function is chosen to have a maximum at $\widetilde{p}_{in,max} = 0.100$Pa, and a minimum at $\widetilde{p}_{in,min} = 1.00 \times 10^{-4}$Pa. $\widetilde{p}_{in,min}$ is set sufficiently small to mitigate any computational issues. We choose $\widetilde{p}_{in,max}$ and $\widetilde{p}_{out}$ based on the measurements of Koch et al. (2004). Considering the measurements corresponding to midday conditions (see Fig. 1a of Koch et al. (2004)), we calculate the slope of the fitted line as approximately $\frac{dP}{dz} = -7.69 \times 10^3$ Pa m^{-1}. Thus, since we consider a vessel section of length $\Delta z = 1.3 \times 10^{-5}$ m, choosing an outlet pressure of 0 Pa, we derive an inlet pressure scale of $\widetilde{p}_{in,max} = \widetilde{p}_{in,min} - \frac{dP}{dz}\Delta z = 0.100$ Pa.

2.4. Initial conditions

To determine the initial biofilm geometry, model equations were run with $\boldsymbol{u}$, Λ, and μ initialised as zero. To make a direct comparison between how different vessels perform under the same level of infection, we initialise ϕ such that the initial biofilm volume is the same across all simulations. Specifically,

$$\phi(x,z) = R(x,z), \tag{34}$$

where R is a random function of uniform distribution. The randomness corresponds to the two phases being initially mixed, *i.e.* we let the organisation evolve according to the physical principles associated with Flory theory. To ensure consistent initial biofilm volume across vessels, R is dependent on vessel size, with mean and range given on the basis of vessel diameter $\widetilde{h}$. Specifically, R is uniformly distributed with mean a and range b defined by

$$a = \frac{b_{vol}H^2}{L\widetilde{h}}, \tag{35}$$

and

$$b = \frac{b_{vol}H^3}{L^2\widetilde{h}}, \tag{36}$$

where H is the chosen characteristic length scale, L is the non-dimensional vessel section length, and b_{vol} controls the initial volume of biofilm. A large value for b_{vol} is chosen to generate aggregate structures resembling *X. fastidiosa* biofilms observed in experimental conditions (De La Fuente et al., 2008). For the main simulations, a low b_{vol} is chosen, corresponding to a small initial amount of biofilm in the domain. We tested running the simulations with three different random initial conditions to ensure the randomness did not affect presented trends. We present the mean and standard deviations of these results.

2.5. Non-dimensionalisation

We non-dimensionalise the model to determine the relative scale of parameters associated with particular processes. The dimensional quantities appearing in the model are length, velocity, pressure, viscosity, growth rate and the various energetic terms. Applied scales for these quantities, chosen to best represent *X. fastidiosa* biofilms in olive xylem vessels, are given in Table 1.

Space is scaled according to $\widetilde{\boldsymbol{x}} = H\boldsymbol{x}$ where H is the average xylem vessel diameter among measurements from susceptible olive cultivars to the nearest μm, taken from Walker et al. (2022). The average fluid velocity through the domain is scaled according to measured xylem sap flow (Fernández et al., 2006); $\widetilde{\boldsymbol{u}} = U\boldsymbol{u}$. We then choose a time scale $\widetilde{t} = \tau t$ associated to these two scales,

$$\tau = \frac{H}{U} = 3.12 \times 10^{-1}. \tag{37}$$

The free-energy density, $\widetilde{f}$, and thus chemical potential, $\widetilde{\mu}$, are non-dimensionalised on the basis of a thermal energy density in accordance with Flory (1953);

$$\Pi = \frac{k_B T}{V_p}. \tag{38}$$

We choose a temperature representative of an annual average across the Puglian region for the value of T, and monomer volume V_p is taken as that used by Wolgemuth et al. (2004). Biofilms contain a range of long chain molecules, and thus χ cannot be determined with any certainty. As such, χ is chosen in accordance to a critical value at which $\widetilde{f}$ experiences a sign change in its second derivative forcing separation. This is discussed further in the Supplementary Information (S3). With the relevant scales, (22) becomes:

$$\Pi\mu = \Pi\partial_\phi f - \frac{\widetilde{\kappa}}{H^2}\nabla^2\phi. \tag{39}$$

This motivates the introduction of a dimensionless biofilm-water correlation energy parameter (see Table 2), defined as

$$\lambda = \frac{\widetilde{\kappa}}{H^2\Pi}. \tag{40}$$

The drag coefficient, $\widetilde{\zeta}$, is difficult to measure for polymers. We observe however that the scalar coefficients in front of each term in (21) correspond to time scales of the represented dynamics. The first, to that of xylem flow, the third, biofilm growth, and the second, biofilm organisation. As such, we choose $\widetilde{\zeta}$ on the basis of the time taken for biofilms to organise, as observed in the experiment of De La Fuente et al. (2008). We choose growth term $\widetilde{G}_1$ to be $G^*\phi$, where G^* represents a biofilm growth rate chosen on the basis of Picioreanu et al. (2000). With relevant scales, (22) becomes:

$$\partial_t\phi + \nabla\cdot\left(\phi\left[\boldsymbol{u} - Pe^{-1}\phi(1-\phi)^2\nabla\mu\right]\right) = \tau G^*\phi, \tag{41}$$

where Pe, a Peclet number, represents the relative importance of advection vs diffusion (see Table 2).

The water-biofilm conversion rate $\widetilde{G}_2$ is also non-dimensionalised

Table 1
List of model parameters for dimensional inputs.

Symbol	Description	Magnitude	Unit	Source
U	Sap flow velocity (velocity scale)	4.17×10^{-5}	ms^{-1}	Estimate on the basis of Fernández et al. (2006)
τ	Experimental organisation time scale	3.12×10^{-1}	s	Assumed $\left(\frac{H}{U}\right)$
τ_{day}	Number of seconds in a day	8.64×10^4	s	Assumed
H	Average Vessel Diameter in Susceptible Olive Cultivars (Length Scale)	1.3×10^{-5}	m	Walker et al. (2022)
L	Vessel Section Length	1.3×10^{-4}	m	Assumed
$\widetilde{\eta}_b$	Biofilm viscosity	400	Pa s	Klapper et al. (2002)
$\widetilde{\eta}_w$	Water viscosity	0.89×10^{-3}	Pa s	Wolgemuth et al. (2004)
k_B	Boltzmann Constant	1.38×10^{-23}	$J K^{-1}$	Daussy et al. (2007)
$\widetilde{\zeta}$	Drag Coefficient between biofilm and water	5×10^{14}	$kg m^{-3} s^{-1}$	Chosen on the basis of De La Fuente et al. (2008)
θ	Biofilm-vessel wall contact angle	$\frac{\pi}{3}$	rad	Lorite et al. (2013)
$\widetilde{\kappa}$	Distortional Energy	5×10^{-9}	N	Transition zone estimated on the basis of Fig. 3b Wolgemuth et al. (2004)
T	Temperature	293.15	K	Assumed
V_p	Volume of polymer section	10^{-24}	m^3	Wolgemuth et al. (2004)
G^*	Biofilm growth rate	1.5×10^{-5}	s^{-1}	Maximum specific growth rate from Picioreanu et al. (2000)
χ	Flory Interaction Parameter	1	–	Critical value, determined in accordance with Doi (2013)
N_x	Number of water molecules between chains in biofilm	10	–	Roose and Fowler (2008)
ϕ_0	Initial EPS fraction	0.03	–	Boudaoud and Chaieb (2003)
$\widetilde{p}_{in,max}$	Maximum pressure at bottom of vessel section	0.100	Pa	Calculated on the basis of Koch et al. (2004)
$\widetilde{p}_{in,min}$	Minimum pressure at bottom of vessel section	1.00×10^{-4}	Pa	Assumed
$\widetilde{p}_{out}$	Pressure at top of vessel section	0	Pa	Calculated on the basis of Koch et al. (2004)
b_{vol}	Initial biofilm volume control factor	10, 1	–	Chosen by comparison with De La Fuente et al. (2008), Assumed

Table 2
Non-dimensional parameter values.

Symbol	Description	Value
Pe^{-1}	Inverse Peclet number	1.49
Ca	Capillary number	7.05×10^{-7}
λ	Dimensionless biofilm-water correlation energy parameter	7.31×10^{-3}

with G^*. In particular, we take $\widetilde{G}_2(\phi)\ [\mathrm{s}^{-1}] = \widetilde{G}_1(\phi)\ [\mathrm{s}^{-1}]$ such that volume is conserved. This is prescribed on the assumption that the volume of the bacteria and polymer chains are negligible, and rather the volume changes are dominated by water becoming immobilised by the EPS matrix. Under this assumption, (24) becomes the divergence free condition

$$\nabla \cdot \boldsymbol{u} = 0. \tag{42}$$

Associated with the free-energy of the system, the Lagrange multiplier $\widetilde{\Lambda}$ and various pressures are non-dimensionalised with Π; $\widetilde{\Lambda} = \Pi\Lambda$, $\widetilde{p}_{out} = \Pi p_{out}$, $\widetilde{p}_{in,max} = \Pi p_{in,max}$ and $\widetilde{p}_{in,min} = \Pi p_{in,min}$. Finally, bulk viscosity $\widetilde{\eta}$ is non-dimensionalised with the viscosity of water $\widetilde{\eta}_w$. Re-writing (23) results in

$$Ca \nabla \cdot \eta\left(\nabla \boldsymbol{u} + (\nabla \boldsymbol{u})^T\right) - \nabla\Lambda = \phi \nabla \mu, \tag{43}$$

where Ca, a capillary number, represents the relative effect of viscous drag forces versus surface tension forces acting at the biofilm-water interface.

The full dimensionless model with prescribed boundary conditions is as follows:

$$\partial_t \phi + \nabla \cdot \left(\phi\left[\boldsymbol{u} - Pe^{-1}\phi(1-\phi)^2 \nabla \mu\right]\right) = \tau G^* \phi, \tag{44}$$

$$\mu = \partial_\phi f - \lambda \nabla^2 \phi, \tag{45}$$

$$\nabla \cdot \eta\left(\nabla \boldsymbol{u} + (\nabla \boldsymbol{u})^T\right) - Ca^{-1}(\nabla\Lambda + \phi\nabla\mu) = 0, \tag{46}$$

$$\nabla \cdot \boldsymbol{u} = 0, \tag{47}$$

$$\boldsymbol{n} \cdot \nabla \mu|_{\Gamma_{wall}} = 0, \tag{48}$$

$$\boldsymbol{n} \cdot \nabla \phi|_{\Gamma_{wall}} = \|\nabla \phi\| \cos\theta, \tag{49}$$

$$\phi|_{\Gamma_{in}} = \phi|_{\Gamma_{out}}, \tag{50}$$

$$\nabla\phi|_{\Gamma_{in}} = \nabla\phi|_{\Gamma_{out}}, \tag{51}$$

$$\Lambda|_{\Gamma_{in}} = p_{in}(t), \tag{52}$$

$$\Lambda|_{\Gamma_{out}} = p_{out}, \tag{53}$$

$$\boldsymbol{u}|_{\Gamma_{wall}} = 0. \tag{54}$$

2.6. Post processing: biofilm and water volume integration

After each simulation is solved, we calculate the volume of biofilm and water passing across the outlet boundary Γ_{out} over the simulation time. The volume of biofilm, $\widetilde{V}_b\ [\mathrm{m}^3]$, is given by

$$\widetilde{V}_b = H^3 \int_0^{t_{end}} \int_{\Gamma_{out}} -\phi\left(Pe \cdot u - \phi(1-\phi)^2 \partial_x \mu\right) \cdot n_x \, dz dt \tag{55}$$

where t_{end} is the non-dimensional simulation run time, $\boldsymbol{n_x}$ is the unit normal perpendicular to the outlet boundary ($x = L$), $\partial_x \mu$ is the derivative of μ with respect to x, u is the x-component of velocity $\boldsymbol{u}$, and z represents the coordinates along the outlet boundary. The volume of water, $\widetilde{V}_w\ [\mathrm{m}^3]$, is given similarly as

$$\widetilde{V}_w = H^3 \int_0^{t_{end}} \int_{\Gamma_{out}} -(1-\phi)\left(Pe \cdot u - \phi^2(1-\phi)\partial_x \mu\right) \cdot n_x \, dz dt. \tag{56}$$

2.7. Simulation protocol

We implemented the model in Comsol Multiphysics v5.5 (2020) using the finite element method (Reddy, 2019). Main simulations were run for two regular meshes, one coarse and one fine, to ensure trends in results were independent of potential mesh effects. Results are presented for fine mesh simulations. Fine meshes had 10 boundary layers on wall boundaries, with a 1.2 stretching factor between layers, and a smooth transition to the interior. The number of interior elements was chosen so that they were consistent in size across the different vessel sizes. Lagrange polynomials of order 2 were used to approximate the solution in each element.

2.7.1. Microfluidic experiment comparison

The domain was scaled to represent the microfluidic chamber in the experiment of De La Fuente et al. (2008), with dimensions $100 \times 140\ \mu\mathrm{m}^2$. The applied fine regular mesh had $130 \times (3 \times round(4h))$ interior elements, where h is the non-dimensional chamber diameter, and $round(\cdot)$ corresponds to the nearest integer value. This resulted in 18,995 total elements. The microfluidic experiment observed biofilm aggregation under no-flow conditions, thus we solve only Eqs. (44), with $\boldsymbol{u} = 0$, (45), (48), (49), (50), and (51). Numerical solutions were saved after every 0.1 s for the first second, every 1 s for the next 99 s, and every 100 s for the last 12,200 s of solution time.

2.7.2. Simulation of biofilm dynamics in different diameter vessels

Multiple simulations of this type were run, scaling the domain according to a range of vessel diameters (between 9.88 μm and 28.6 μm) after Walker et al. (2022). All vessel sections were given length $L = 130\ \mu$m. The course mesh prescribed $80 \times (2 \times round(5h))$ elements, with no boundary layers. The fine mesh prescribed $120 \times (3 \times round(4h))$ interior elements, resulting in 3480 quadrilateral surface elements for the smallest, and 5640 for the largest diameter vessel. Numerical solutions to the full set of model equations (Eqs. (44)-(54)) were saved after every 10000 s of solution time up to the specified stopping condition.

2.8. Stopping condition

Simulations were run up until the first time biofilm spanned the outlet boundary. Specifically, until the minimum of ϕ on the outlet boundary exceeded 0.5. We chose 0.5 rather than 0 to distinguish between initial times where the biofilm is diffuse throughout the domain.

2.9. Analytic flow under healthy conditions

We calculate the flow through each vessel under healthy conditions to compare with modelled flow under infection. For a planar Poiseuille flow, the nondimensional volumetric flow rate per unit depth normal to the plane of the flow is given by

$$q = \frac{h^3 Ca^{-1}}{12}\left(-\frac{\partial p}{\partial x}\right). \tag{57}$$

The solution for the volume of water $\widetilde{V}\ [\mathrm{m}^3]$ passing through a vessel of diameter $\widetilde{h}\ [\mathrm{m}]$ over non-dimensional simulation time t_{end} is

$$\widetilde{V} = H^3 \int_0^{t_{end}} q dt = \frac{\widetilde{h}^3 Ca^{-1}}{12L} \left[\frac{\left(p_{in,max} - p_{in,min}\right)}{2} t_{end} + \frac{\left(p_{in,max} + p_{in,min}\right)\tau_{day}}{4\pi\tau} cos\left(\frac{2\pi\tau t_{end}}{\tau_{day}} - \frac{\pi}{2}\right) \right]. \quad (58)$$

3. Results

3.1. Aggregation pattern validation

Structures formed by modelled biofilm organisation (Fig. 2a, 2c), Eqs. (44), (45), (48), (49), (50), (51)), were compared to *X. fastidiosa* biofilms aggregating in a microfluidic chamber (Fig. 2b, 2d (De La Fuente et al., 2008)) under no-flow conditions, starting from a random initial configuration (Fig. 2a, 2b (De La Fuente et al., 2008)). Presented biofilm aggregation patterns are those observed over a time period of ~ 1 h; a time scale specific to the organisation dynamics. The model captures the same aggregation behaviour observed in the experiment (Fig. 2b, 2d).

3.2. Diurnal cycles

At night, a very small pressure gradient ensures negligible sap flow. In these conditions, biofilm aggregation occurs passively driven by the polymer physics (Fig. 3a). During the day, the pressure gradient becomes significant, and xylem sap is forced through the vessel. This has the effect of pushing biofilm through the vessel and smoothening the biofilms on the vessel walls (Fig. 3b).

3.3. 100 day simulations: effect of vessel diameter on biofilm spread

We ran simulations to investigate the effect of vessel diameter on the total biofilm volume moved through the vessel until the outlet is spanned by biofilm (videos of select simulations are available, as described in Supplementary Information S6). Results (Eq. (55)) show that wider vessels achieve greater fluxes of biofilm, in particular, the relationship suggests the criticality of the largest vessels in facilitating pathogen spread in the vasculature (Fig. 4).

3.4. 100 day simulations: effect of vessel diameter on reduction in hydraulic conductivity under infection

We ran simulations to investigate the effect of vessel diameter on the reduction in hydraulic conductivity of infected vessels. The water volume passing through model vessels up to the point of biofilm spanning the outlet width was obtained from the simulations (Eq. (56)). We compared the result to that assuming a healthy vessel conducting water over the same time period (Eq. (58)). Results show that though the widest vessels still conduct the most water, all vessels experience a significant loss in hydraulic functionality, 2–3 orders of magnitude, under infection (Fig. 5).

3.5. 100 day simulations: biofilm spread in the vasculature of different olive cultivars

Integrating the volume of biofilm through each modelled diameter vessel with the vessel size distributions of four olive cultivars measured by Walker et al. (2022), we present a predicted relative cumulative spread of biofilm through vessels of different diameter in the vasculature of each cultivar (Fig. 6). Overall spread is dominated by the presence of wider vessels. Even though they are still in relatively low abundance, plants of susceptible cultivar Koroneiki have proportionally more wide vessels than the other cultivars, and thus our results predict proportionally more pathogen spread. In contrast, resistant Leccino plants have much fewer wide vessels.

4. Discussion

Xylem-limited plant vascular diseases are among the most destructive diseases occurring in crops (Yadeta et al., 2013). However, current understanding of how infection progresses within the plant host is limited. Modelling could provide an avenue with which to gain important insights. Models developed to investigate dynamics associated to biofilms in plant vasculature are presented in the literature (Cogan et al.,

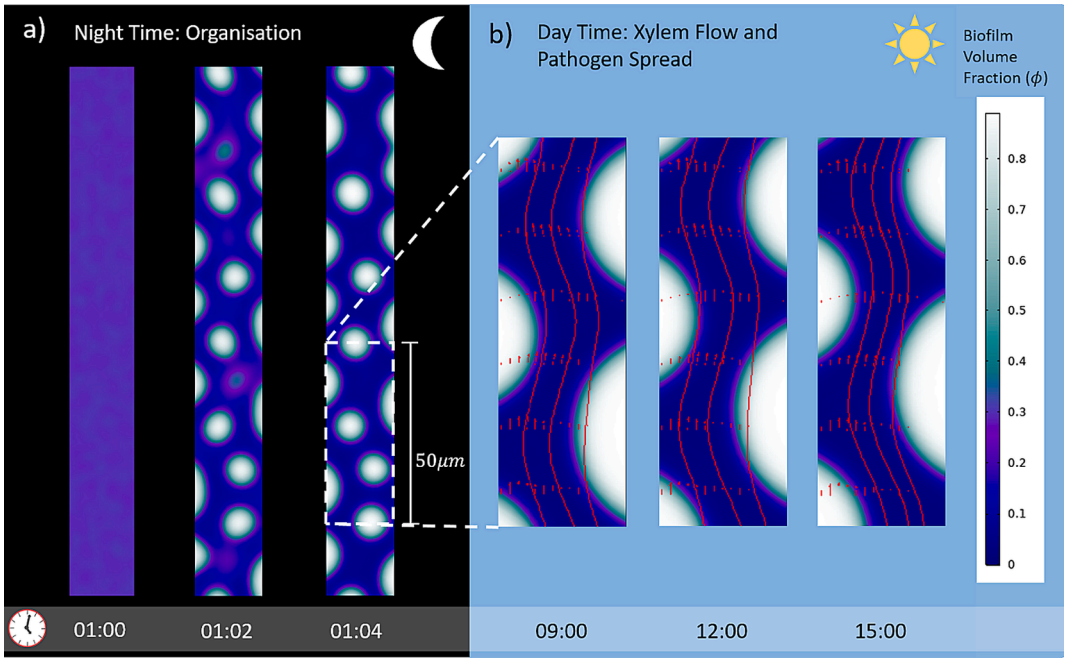

Fig. 3. Day and Night Biofilm Dynamics. This simulation, used to illustrate the dynamics, was initialised with a high biofilm volume.

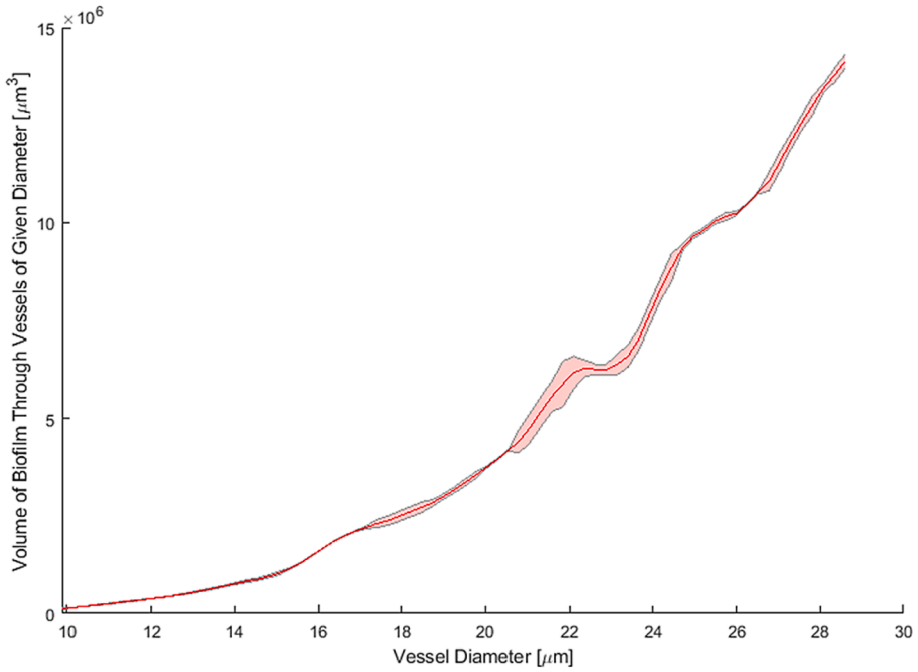

Fig. 4. Mean Volume of Biofilm Moved Through Vessels of Varying Diameter Over a Time Period of 100 Days. Simulations were run for three different initial conditions (n = 3). The shaded region represents the standard deviation of the results.

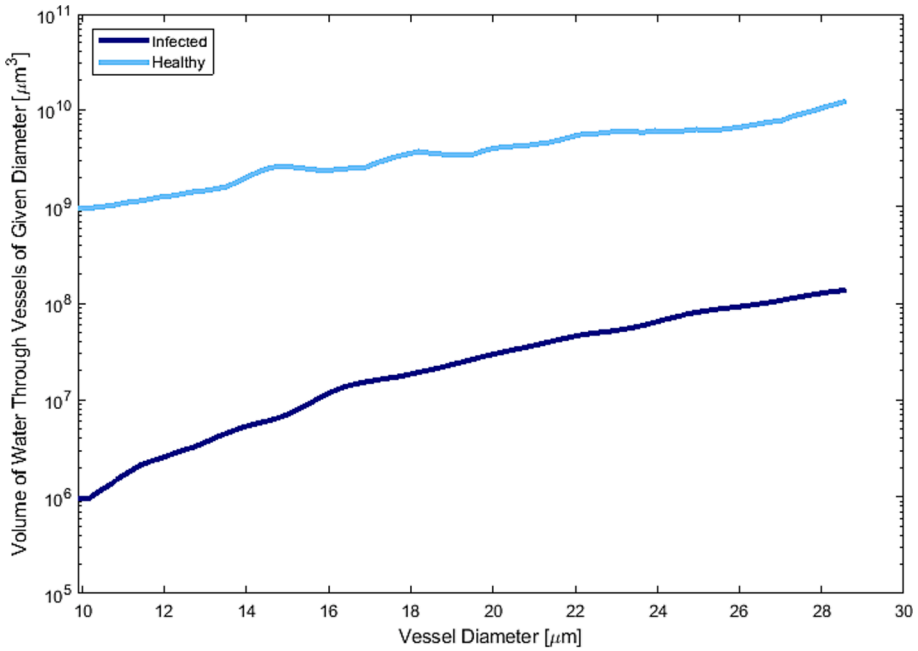

Fig. 5. Volume of Water Through Vessels of Varying Diameter Over a Time Period of 100 Days. Water volumes are compared with those passing through the corresponding healthy vessel over the same time period.

2013; Whidden et al., 2015). However, due to their complexity, model solutions could only be considered under static flow conditions, and thus, could not capture key dynamics associated to realistic flow regimes. General biofilm models that describe biofilm structure and growth in fluid environments have been presented in the literature (Klapper and Dockery, 2002; Cogan and Keener, 2004; Cogan and Keener, 2005; Zhang et al., 2008; Zhang et al., 2008; Cogan and Guy, 2010; Winstanley et al., 2011). However, limitations to these models remain in regards to applied dimensionality reduction, robust representation of key parameters, and computational complexity. In this study, we develop a general theoretical model of biofilm dynamics within xylem vessels, capturing the interaction between biofilm and dynamic sap flow with minimal reliance on experimental parameters. We then used the model to investigate a number of hypotheses pertaining to mechanisms of olive cultivar resistance to *Xylella fastidiosa*.

To carry out our investigation, both model parameters and applied boundary conditions were selected to best represent what has been measured for *X. fastidiosa* biofilms. Simulation results were compared with *X. fastidiosa* aggregation patterns observed in a micro-fluidic chamber (De La Fuente et al., 2008; Fig. 2). Starting from a random

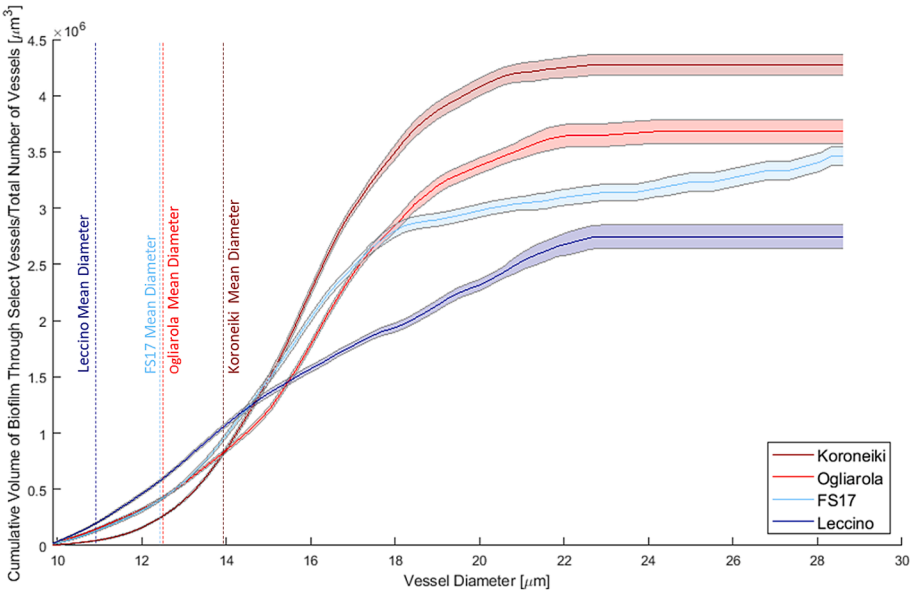

Fig. 6. Mean Biofilm Spread in the Vasculature of Four Different Cultivars. The shaded regions represent the standard deviation (n = 3). Cultivars Leccino and FS17 are resistant to *X. fastidiosa*, whilst Koroneiki and Ogliarola are susceptible.

field configuration, a simulation captured the same aggregation patterns as observed in the experiment. As well as acting as a model validation, this result suggests that biofilm aggregation in xylem vessels under idealised conditions is well characterised by polymer physics. Many studies relating to bacterial plant vascular pathogens focus on the biological complexities associated with community driven bacterial behaviour (Karunakaran et al., 2011). Here we provide evidence that important dynamics relevant to disease development can be understood without this complexity.

Though previous modelled biofilm structures have been compared under flow and 'no flow' conditions (Zhang et al., 2008), dynamics under diurnal pressure conditions have not been considered, neglecting characteristic fluctuations in dynamics occurring in plant xylem (Fig. 3). We used our model, with implemented diurnal pressure condition, to investigate the effect of xylem vessel diameter on biofilm transport and loss of vessel functionality under infection. Our results show that under infection, all vessels experience a significant reduction in hydraulic conductivity regardless of their diameter (Fig. 5). In addition, we found that wider vessels achieved greater fluxes of biofilm (Fig. 4). In particular, the non-linear relationship between vessel diameter and biofilm transport suggests the importance of the largest vessels in facilitating pathogen spread (Fig. 4). Several cases have been described in which olive cultivar resistance to *X. fastidiosa* is related to smaller vessels (Chatelet et al., 2011; Sabella et al., 2019; Petit et al., 2021; Walker et al., 2022). Though theoretical evidence for the higher susceptibility of wider vessels to air embolism has been provided by Petit et al. (2021) and Walker et al. (2022), the effect of vessel diameter on pathogen spread could not be addressed, and has not previously been investigated. This work provides a physical mechanism by which wider vessels could have a significant effect on pathogen spread.

Finally, we relate model results to the distributions of vessels in cultivars of different susceptibility to *X. fastidiosa* (Walker et al., 2022). In doing so, we predict a relative greater spread of biofilm in the vasculature of olive cultivars Koroneiki, Ogliarola and FS17 in comparison with Leccino. This difference is dictated by the faster flow and late biofilm bridging in the widest vessels, which are absent in Leccino plants. Despite these wide vessels being found in low abundance in all cultivars, Fig. 6 shows that where they are present, their influence on pathogen spread is still significant. Though powerful on its own, this result could be strengthened with information from high resolution images, providing details of vessel connections in the vasculature of the respective cultivars. It is these connections that dictate inter-vessel movement of the pathogen. Image-based modelling, a technique which uses images to construct model geometries, is a powerful approach for considering the function of complex biological structures. With appropriate data, future studies can expand on our model to explicitly consider biofilm development within real vessel geometries and estimate bacterial spreading between vessels. These *in silico* experiments will provide further evidence into the way in which vascular geometries influence disease development.

Applying our model to the context of the olive quick decline syndrome, we provide evidence that it is the relative dominance of larger vessels to the pore space of susceptible cultivars that has a significant influence on biofilm spread. In particular, results suggest pathogen spread is limited by the lack of large vessels in Leccino. As such, we suggest that a xylem morphological screening may be useful to identify resistant cultivars. However, predicted spread in the vasculature of susceptible Ogliarola compared with resistant FS17 was roughly comparable. We anticipate that the resistance of FS17 may instead be dominated by other non-geometric factors; for example, genetic factors (Choi et al., 2013; Giampetruzzi et al., 2016), factors relating to xylem chemical composition (Sabella et al., 2018), or those relating to the management of the defence response (De Benedictis et al., 2017). Thus, we suggest future screening protocols should include multiple stages of which xylem morphology would constitute only one stage.

Declaration of competing interest

The authors declare that they have no known competing financial interests or personal relationships that could have appeared to influence the work reported in this paper.

Acknowledgements

Authors would like to acknowledge Dr Arpan Ghosh for his contributions to early discussions regarding the modelling approach.

NCW and TR are funded by NERC grant NE/S00720/1. SMW is funded by the European Union's Horizon 2020 Research and Innovation Programme under grant agreement number 727987–XF-ACTORS "Xylella Fastidiosa Active Containment Through a Multidisciplinary-Oriented Research Strategy", the grant agreement number 734353–CURE-XF "Capacity Building and Raising Awareness in Europe

and in Third Countries to Cope with Xylella fastidiosa" and by the BRIGIT project by UK Research and Innovation through the Strategic Priorities Fund, by a grant from Biotechnology and Biological Sciences Research Council, with support from the Department for Environment, Food and Rural Affairs and the Scottish Government (BB/S016325/1). SR, DMF and TR are funded by ERC Consolidator grant 646809 (Data Intensive Modelling of the Rhizosphere Processes). SR was also funded by BBSRC Discovery Fellowship BB/X010147/1 and Royal Society University Research Fellowship URF\R1\231622, and DMF by the Rural and Environment Science and Analytical Services Division (SRUC-C5-1). MS is funded by the European Union's Horizon 2020 Research and Innovation Programme under grant agreement number 727987–XF-ACTORS, and the grant agreement number 635646–POnTE "Pest Organisms Threatening Europe".

Appendix A. Supplementary data

Supplementary data to this article can be found online at https://doi.org/10.1016/j.jtbi.2024.111737.

References

Agrios, G.N., 2005. Plant pathology. Elsevier.
Boudaoud, A., Chaieb, S., 2003. Mechanical phase diagram of shrinking cylindrical gels. Phys. Rev. E 68, 021801.
Bové, J., Garnier, M., 2002. Phloem-and xylem-restricted plant pathogenic bacteria. Plant Sci. 163, 1083–1098.
Chatelet, D.S., Wistrom, C.M., Purcell, A.H., Rost, T.L., Matthews, M.A., 2011. Xylem structure of four grape varieties and 12 alternative hosts to the xylem-limited bacterium *Xylella fastidious*. Ann. Bot. 108, 73–85.
Choi, H.-K., Iandolino, A., da Silva, F.G., Cook, D.R., 2013. Water deficit modulates the response of *Vitis vinifera* to the Pierce's disease pathogen *Xylella fastidiosa*. Mol. Plant Microbe Interact. 26, 643–657.
Cogan, N., Donahue, M., Whidden, M., De La Fuente, L., 2013. Pattern formation exhibited by biofilm formation within microfluidic chambers. Biophys. J. 104, 1867–1874.
Cogan, N., Guy, R.D., 2010. Multiphase flow models of biogels from crawling cells to bacterial biofilms. HFSP Journal 4, 11–25.
Cogan, N., Keener, J.P., 2004. The role of the biofilm matrix in structural development. Math. Med. Biol.: J. IMA 21, 147–166.
Cogan, N., Keener, J.P., 2005. Channel formation in gels. SIAM J. Appl. Math. 65, 1839–1854.
2020 COMSOL Multiphysics® v. 5.5. (www.comsol.com), COMSOL AB, Stockholm, Sweeden.
Daussy, C., Guinet, M., Amy-Klein, A., Djerroud, K., Hermier, Y., Briaudeau, S., Bordé, C. J., Chardonnet, C., 2007. Direct determination of the Boltzmann constant by an optical method. Phys. Rev. Lett. 98, 250801.
De Benedictis, M., De Caroli, M., Baccelli, I., Marchi, G., Bleve, G., Gallo, A., Ranaldi, F., Falco, V., Pasquali, V., Piro, G., 2017. Vessel occlusion in three cultivars of *Olea europaea* naturally exposed to *Xylella fastidiosa* in open field. J. Phytopathol. 165, 589–594.
De La Fuente, L., Burr, T.J., Hoch, H.C., 2008. Autoaggregation of Xylella fastidiosa cells is influenced by type I and type IV pili. Appl. Environ. Microbiol. 74, 5579–5582.
Dixon, H.H., Joly, J., 1895. XII. On the ascent of sap. Philos. Trans. R. Soc. Lond. B, 563–576.
Doi, M., 2013. Soft matter physics. Oxford University Press.
Donlan, R.M., 2002. Biofilms: microbial life on surfaces. Emerg. Infect. Dis. 8, 881.
Eberl, H.J., Parker, D.F., Vanloosdrecht, M.C., 2001. A new deterministic spatio-temporal continuum model for biofilm development. Comput. Math. Methods Med. 3, 161–175.
Eberl, H., Picioreanu, C., Heijnen, J., Van Loosdrecht, M., 2000. A three-dimensional numerical study on the correlation of spatial structure, hydrodynamic conditions, and mass transfer and conversion in biofilms. Chem. Eng. Sci. 55, 6209–6222.
Evans, L.V., 2000. Biofilms: recent advances in their study and control. CRC Press.
Fernández, J., Durán, P., Palomo, M., Diaz-Espejo, A., Chamorro, V., Girón, I., 2006. Calibration of sap flow estimated by the compensation heat pulse method in olive, plum and orange trees: relationships with xylem anatomy. Tree Physiol. 26, 719–728.
Flory, P.J., 1953. Principles of polymer chemistry. Cornell University Press.
Giampetruzzi, A., Morelli, M., Saponari, M., Loconsole, G., Chiumenti, M., Boscia, D., Savino, V.N., Martelli, G.P., Saldarelli, P., 2016. Transcriptome profiling of two olive cultivars in response to infection by the CoDiRO strain of *Xylella fastidiosa* subsp. *pauca*. BMC Genomics 17, 1–18.
Hall-Stoodley, L., Costerton, J.W., Stoodley, P., 2004. Bacterial biofilms: from the natural environment to infectious diseases. Nat. Rev. Microbiol. 2, 95–108.
Hillert, M., Ågren, J., 2006. Extremum principles for irreversible processes. Acta Mater. 54, 2063–2066.
Karunakaran, E., Mukherjee, J., Ramalingam, B., Biggs, C.A., 2011. "Biofilmology": a multidisciplinary review of the study of microbial biofilms. Appl. Microbiol. Biotechnol. 90, 1869–1881.
Kearns, D.B., 2010. A field guide to bacterial swarming motility. Nat. Rev. Microbiol. 8, 634–644.
Klapper, I., Dockery, J., 2002. Finger formation in biofilm layers. SIAM J. Appl. Math. 62, 853–869.
Klapper, I., Rupp, C.J., Cargo, R., Purvedorj, B., Stoodley, P., 2002. Viscoelastic fluid description of bacterial biofilm material properties. Biotechnol. Bioeng. 80, 289–296.
Koch, G.W., Sillett, S.C., Jennings, G.M., Davis, S.D., 2004. The limits to tree height. Nature 428, 851–854.
Krishnan, H.B., Natarajan, S.S., Bennett, J.O., Sicher, R.C., 2011. Protein and metabolite composition of xylem sap from field-grown soybeans (Glycine max). Planta 233, 921–931.
Lorite, G.S., Janissen, R., Clerici, J.H., Rodrigues, C.M., Tomaz, J.P., Mizaikoff, B., Kranz, C., de Souza, A.A., Cotta, M.A., 2013. Surface physicochemical properties at the micro and nano length scales: role on bacterial adhesion and Xylella fastidiosa biofilm development. PLoS One 8, e75247.
Mansfield, J., Genin, S., Magori, S., Citovsky, V., Sriariyanum, M., Ronald, P., Dow, M., Verdier, V., Beer, S.V., Machado, M.A., 2012. Top 10 plant pathogenic bacteria in molecular plant pathology. Mol. Plant Pathol 13, 614–629.
Mattick, J.S., 2002. Type IV pili and twitching motility. Annu. Rev. Microbiol. 56, 289–314.
Onsager, L., 1931a. Reciprocal relations in irreversible processes. I. *Physical Review* 37, 405.
Onsager, L., 1931b. Reciprocal relations in irreversible processes. II. *Physical Review* 38, 2265.
Petit, G., Bleve, G., Gallo, A., Mita, G., Montanaro, G., Nuzzo, V., Zambonini, D., Pitacco, A., 2021. Susceptibility to *Xylella fastidiosa* and functional xylem anatomy in *Olea europaea*: revisiting a tale of plant–pathogen interaction. AoB Plants 13, plab027.
Picioreanu, C., Van Loosdrecht, M.C., Heijnen, J.J., 2000. Effect of diffusive and convective substrate transport on biofilm structure formation: A two-dimensional modeling study. Biotechnol. Bioeng. 69, 504–515.
Rapicavoli, J., Ingel, B., Blanco-Ulate, B., Cantu, D., Roper, C., 2018. Xylella fastidiosa: an examination of a re-emerging plant pathogen. Mol. Plant Pathol 19, 786–800.
Reddy, J.N., 2019. Introduction to the finite element method. McGraw-Hill Education.
Roose, T., Fowler, A.C., 2008. Network development in biological gels: role in lymphatic vessel development. Bull. Math. Biol. 70, 1772–1789.
Sabella, E., Luvisi, A., Aprile, A., Negro, C., Vergine, M., Nicolì, F., Miceli, A., De Bellis, L., 2018. *Xylella fastidiosa* induces differential expression of lignification related-genes and lignin accumulation in tolerant olive trees cv. Leccino. J. Plant Physiol. 220, 60–68.
Sabella, E., Aprile, A., Genga, A., Siciliano, T., Nutricati, E., Nicolì, F., Vergine, M., Negro, C., De Bellis, L., Luvisi, A., 2019. Xylem cavitation susceptibility and refilling mechanisms in olive trees infected by *Xylella fastidiosa*. Sci. Rep. 9, 1–11.
Saponari, M., Boscia, D., Nigro, F., Martelli, G.P., 2013. Identification of DNA sequences related to Xylella fastidiosa in oleander, almond and olive trees exhibiting leaf scorch symptoms in Apulia (Southern Italy). J. Plant Pathol. 95.
Saponari, M., Giampetruzzi, A., Loconsole, G., Boscia, D., Saldarelli, P., 2019. *Xylella fastidiosa* in olive in Apulia: Where we stand. Phytopathology 109, 175–186.
Sternberg, C., Christensen, B.B., Johansen, T., Toftgaard Nielsen, A., Andersen, J.B., Givskov, M., Molin, S., 1999. Distribution of bacterial growth activity in flow-chamber biofilms. Appl. Environ. Microbiol. 65, 4108–4117.
Vidhyasekaran, P., 2002. Bacterial disease resistance in plants: molecular biology and biotechnological applications. CRC Press.
Walker, N., White, S., McKay Fletcher, D., Ruiz, S., Rankin, K., De Stradis, A., Saponari, M., Williams, K., Petroselli, C. & Roose, T. 2022 The Impact of Xylem Geometry on Olive Cultivar Resistance to Xylella fastidiosa: An Image-based Study. *Plant Pathology*.
Whidden, M., Cogan, N., Donahue, M., Navarrete, F., De La Fuente, L., 2015. A Two-Dimensional Multiphase Model of Biofilm Formation in Microfluidic Chambers. Bull. Math. Biol. 77, 2161–2179.
Winstanley, H., Chapwanya, M., McGuinness, M., Fowler, A.C., 2011. A polymer–solvent model of biofilm growth. Proceedings of the Royal Society a: Mathematical, Physical and Engineering Sciences 467, 1449–1467.
Wolgemuth, C.W., Mogilner, A., Oster, G., 2004. The hydration dynamics of polyelectrolyte gels with applications to cell motility and drug delivery. Eur. Biophys. J. 33, 146–158.
Yadeta, K.A., Thomma, J., 2013. The xylem as battleground for plant hosts and vascular wilt pathogens. Front. Plant Sci. 4, 97.
Zhang, T., Cogan, N.G., Wang, Q., 2008. Phase field models for biofilms. I. Theory and one-dimensional simulations. SIAM J. Appl. Math. 69, 641–669.
Zhang, T., Cogan, N., Wang, Q., 2008. Phase-field models for biofilms II. 2-D numerical simulations of biofilm-flow interaction. Commun. Comput. Phys 4, 72–101.